

Nanogymnastics: Visualization of Intercluster Reactions by High-Resolution Trapped Ion Mobility Mass Spectrometry

Ananya Baksi,^{†,‡,§} Erik Karsten Schneider,[‡] Patrick Weis,^{‡,§} K. R. Krishnadas,[§] Debasmita Ghosh,[§] Horst Hahn,^{*,†} Thalappil Pradeep,^{*,§} and Manfred M. Kappes^{*,†,‡,§}

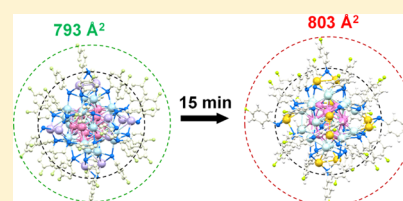
[†]Institute of Nanotechnology, Karlsruhe Institute of Technology, 76344 Eggenstein-Leopoldshafen, Baden-Württemberg, Germany

[‡]Institute of Physical Chemistry, Karlsruhe Institute of Technology, 76131 Karlsruhe, Baden-Württemberg, Germany

[§]DST Unit of Nanoscience and Thematic Unit of Excellence, Indian Institute of Technology Madras, Chennai, Tamil Nadu 600036, India

Supporting Information

ABSTRACT: Although single-crystal X-ray diffraction is a proven technique to determine the structure of monolayer-protected coinage metal clusters in solid state, it is not readily applicable to the characterization of such cluster structures in solution. The complexity of the characterization problem increases further when *intercluster* reactions are studied, in which two reactive cluster ions interact to form final products using a sequence of structural changes involving exchange of metal atoms and ligands. Here, we present the first time-resolved structural study of such processes which occur when solutions of $[\text{TOA}]^+[\text{Au}_{25}(\text{PET})_{18}]^-$ and $[\text{PPh}_4]_4^+[\text{Ag}_{44}(\text{FTP})_{30}]^{4-}$ react upon mixing (PET: phenylethanethiolate; FTP: 4-fluorothiophenolate; and TOA: tetraoctylammonium ion). This is achieved using high-resolution trapped ion mobility mass spectrometry (TIMS). Specifically, we have used electrospray transfer to the TIMS apparatus followed by ion mobility measurements to probe the time-dependent structure of mass-selected $\text{Au}_x\text{Ag}_{44-x}(\text{FTP})_{30}^{4-}$ ($x = 0-12$) exchange products, with limited FTP for PET exchanges, formed in the reaction medium. Over the roughly 40 min reaction time before equilibration, with a product distribution centered around $\text{Au}_{12}\text{Ag}_{32}(\text{FTP})_{30}^{4-}$, we observe intermediate species, $\text{Au}_x\text{Ag}_{44-x}(\text{FTP})_{30}^{4-}$, whose collision cross sections (CCSs) at a given x increase first relative to that of the $\text{Ag}_{44}(\text{FTP})_{30}^{4-}$ parent and decrease subsequently. We attribute this to an energy-driven migration of the incorporated Au atoms from the ligated “staples” at the cluster surface to its icosahedral core. Upon collisional heating of $\text{Au}_x\text{Ag}_{44-x}(\text{FTP})_{30}^{4-}$, analogous back-migration of the heavier Au atoms from the core to the staples was observed in tandem mass spectrometry. To support our experimental observations, several isomeric structures (with all ligands) were calculated using density functional theory, and their CCS values were modeled using trajectory method calculations.



1. INTRODUCTION

The size-dependent chemical physics of unprotected and therefore extremely reactive atomically precise metal clusters has been studied systematically in molecular beams for more than 50 years.^{1–4} By contrast, it is only after the development of scalable cluster growth and monolayer protection about 20 years ago that a homologous series of ligand-protected homometallic clusters with a wide range of differently sized cores became available to mainstream chemistry.^{5–8} Among clusters of coinage metals, these approaches were first developed for gold and later extended to silver and copper. Most recently, monolayer-protected bimetallic alloy nanoclusters comprising all coinage metals have also become available. Monolayer-protected, atomically precise, core–shell bimetallic nanoclusters are presently of great interest because of their unique shape and size-/composition-dependent reactivity.^{9–13} Being size-selected with atomic precision, bimetallic clusters have a measurable molecular formula and can thus be considered as bridges between metal alloy nanoparticles and the (smaller) molecular regime.¹⁴

Synthesis of monolayer-protected alloy clusters is generally carried out by using two different metal precursors which react to form a new alloy cluster with defined nuclearity and composition.¹⁵ In many cases, the position of the heteroatom(s) is analyzed by X-ray crystallography.^{16,17} Galvanic and antgalvanic exchange has also been used to dope a single or a few heteroatoms (also noncoinage metals) into the presynthesized homonuclear clusters. Adding metal thiolates to a homonuclear cluster followed by reduction using NaBH_4 has also been shown to allow the formation of alloy clusters.^{17–21}

A newly emerging technique to make alloy clusters which has attracted a lot of attention recently is intercluster reactions.^{12,13,22–25} Remarkably, two atomically precise homonuclear clusters, each containing a different coinage metal, can interact with each other in solution under ambient conditions to form alloy clusters by exchange of metals and ligands. Various types of interactions have been reported,^{26,27} leading

Received: September 12, 2019

Revised: October 24, 2019

Published: October 27, 2019



to both alloys with variable atomic compositions—without changing the overall nuclearities of the respective cores—and dimers.^{13,26} Recent reports of such reactions between Ag and Au clusters have shown rapid exchange of Au/Ag in the respective clusters independent of whether the reactant species have the same or different nuclearities. The first such report showed reaction between $\text{Ag}_{44}(\text{SR})_{30}$ clusters with $\text{Au}_{25}(\text{SR})_{18}$ clusters being added to the same solution (where SR corresponds to one of several different possible thiolate ligands). This was probed by UV–vis absorption spectroscopy and mass spectrometry.^{23,24} Although multiple Ag atom exchanges were seen in the gold cluster upon adding a small amount of $\text{Ag}_{44}(\text{SR}')_{30}$ to an excess of $\text{Au}_{25}(\text{SR})_{18}$, up to 12 Au atoms were found to be exchanged into the $\text{Ag}_{44}(\text{SR}')_{30}$ cluster in parallel—along with the exchange of a few ligands on both sides. Density functional theory (DFT) calculations of the corresponding energetics suggested that eventually all the 12 Au atoms should go to the icosahedral core of the 44-atom cluster, which is the most stable substitutional isomer of $\text{Au}_{12}\text{Ag}_{32}(\text{SR})_{30}$.²³ The cluster consists of six ligand-terminated “staples” comprising two silver atoms (and five ligands) each. The staples sit on top of a 20-atom shell of silver atoms which in turn contains a 12-atom hollow icosahedral core of gold atoms (i.e., without a central atom).

The DFT structure is in agreement with the crystal structure of $\text{Au}_{12}\text{Ag}_{32}(\text{SR})_{30}$ directly prepared from mononuclear precursors by Zheng et al.^{28,29} In a recent report of alloy clusters formed in a related “one-pot ab initio synthesis”, Zheng et al. showed by X-ray crystallography that any number of Au doping (from 0 to 12) in $\text{Ag}_{44}(\text{SR})_{30}$ clusters leads to Au exchange in the icosahedral core.²⁹ By contrast, Xie et al. have suggested that 12 Au atoms exchange on the surface (staple) of the preformed $\text{Ag}_{44}(\text{SR})_{30}$ clusters (rather than in its core) when the exchange is mediated by $\text{Au}(\text{SR})_2\text{Cl}$ -type thiolates.³⁰ In a related study, Bürgi et al. have inferred that over longer times, silver exchange occurs preferentially in the core of a $\text{Au}_{38}(\text{SR})_{24}$ cluster rather than on its staples.³¹

Although the latter studies give some first information about the structural consequences of the exchange reaction, they do not provide extensive insight into its mechanism. In all cases of Au exchange into preformed silver clusters, it seems clear that the reaction must start from the outside, that is, start at the staples with the exchanged Au atoms perhaps subsequently migrating to the core. If this is indeed the case, then the associated rearrangement process must be associated with transitory volume and packing changes as the molecule isomerizes in a “nanogymnastics” fashion to allow for subsurface diffusional exchange. The comparatively high mobility of coinage metal atoms in such clusters under ambient conditions is highlighted in a recent report by Pradeep et al. who showed that rapid exchange between Ag^{107} and Ag^{109} (to the respective statistical limits) can happen when mixing the two corresponding isotopically pure clusters—for both $\text{Ag}_{25}(\text{SR})_{18}$ and $\text{Ag}_{29}(\text{SR})_{12}$.³²

In the present study, we show the first time-resolved visualization of the structural changes of $\text{Ag}_{44}(\text{SR})_{30}$ cluster ions (SR = FTP; 4-fluorothiophenolate) during intercluster reaction with $\text{Au}_{25}(\text{SR})_{18}$ cluster (SR' = PET; phenylethanethiolate). We obtain this information using high-resolution trapped ion mobility mass spectrometry (TIMS) coupled with electrospray ionization (ESI) to probe solution composition at selected times after starting the exchange reaction.^{33–37} We show that the initial interaction of the

$\text{Ag}_{44}(\text{FTP})_{30}$ clusters with $\text{Au}_{25}(\text{PET})_{18}$ leads to distortion/expansion of the $\text{Ag}_{44}(\text{FTP})_{30}$ precursors as Ag/Au exchange proceeds. By analyzing all of the intermediate ions, we were able to probe the concerted migration mechanism transporting Au atoms from the surface to the cluster core (and correspondingly silver atoms from core to the surface). Collision-induced dissociation (CID) measurements of the Au-exchanged ions show that as the Au content of the system increases, Au can also diffuse back to the surface of the energized clusters—as indicated by the respective Au-containing fragments. To support the inferences from TIMS measurements, DFT was used to calculate (isomeric) structures of selected $\text{Au}_x\text{Ag}_{44-x}(\text{FTP})_{30}^{4-}$ species ($x = 0–12$). These DFT structures in turn formed the basis for trajectory method (TM) calculations, which were used to model the collision cross sections (CCSs) resulting from the ion mobility measurements.

2. EXPERIMENTAL SECTION

2.1. Synthesis Details. The clusters $\text{Au}_{25}(\text{PET})_{18}$ ³⁸ and $[\text{PPh}_4]_4[\text{Ag}_{44}(\text{FTP})_{30}]$ ³⁷ were synthesized and characterized following the previously reported methods (see the Supporting Information for details and Figures S1 and S2).

2.2. Instrumental Details. The time dependence of intercluster reactions in solution was studied by recording the ESI mass spectra using three different mass spectrometers, namely, a Bruker timsTOF, a Thermo Fisher Orbitrap, and a Waters SYNAPT G2S HDMS. In spite of the different ESI sources and spray conditions used, mass spectra were in good qualitative agreement across the three different platforms. The SYNAPT was used for CID measurements. The timsTOF was used to obtain ^{TIMS}CCS_{N₂} values. Details of the instruments and typical operating parameters are also given in the Supporting Information.

2.3. Computational Details. All ion geometries were obtained using DFT with the BP-86 functional^{39,40} and the def-SV(P) basis set⁴¹ as implemented in the TURBOMOLE⁴² package. We used the experimental geometry (X-ray structure) of $[\text{PPh}_4]_4[\text{Ag}_{44}(\text{FTP})_{30}]$ as the starting point and removed the $[\text{PPh}_4]^+$ counterions to obtain an initial $\text{Ag}_{44}(\text{FTP})_{30}^{4-}$ structure. This structure was then fully optimized without any symmetry restrictions. For the mixed Au/Ag systems, we replaced the respective silver atoms by gold atoms in the optimized structure and performed a new geometry optimization, again without symmetry restrictions. Partial charges on each atom (necessary for the CCS calculation) were assigned with a natural bond orbital (NBO) population analysis⁴³ unless otherwise noted. The optimized ion geometries and partial charges (see Tables S1–S4) formed the basis of systematic TM calculations as implemented in the IMoS 1.09 package.^{44,45} For each CCS, we ran 3×10^6 trajectories at a temperature of 300 K with the “carbon first” optimized Lennard-Jones parameters of Wu et al.,⁴⁶ that is, the default parameters of IMoS 1.09.

3. RESULTS AND DISCUSSION

The reaction kinetics of Au exchange and the resulting formation of $\text{Au}_x\text{Ag}_{44-x}(\text{SR})_{30}^{4-}$ cluster ions, $x = 1–12$ (SR = FTP or PET)²³ were monitored in-line generally using a high-resolution trapped ion mobility mass spectrometer (Bruker timsTOF) equipped with an ESI source. Dilute solutions (10 μM and below) of both $[\text{PPh}_4]_4[\text{Ag}_{44}(\text{FTP})_{30}]$ and $[\text{TOA}]$ -

[Au₂₅(PET)₁₈] were mixed in dimethyl formamide solvent and the products formed under ambient conditions were monitored continuously (at a temperature of ca. 298 K). We estimate the “dead time” between the start of the reaction upon mixing and the earliest timsTOF detection of products to be about 60 s. Note that we have optimized the ESI source conditions such that Au_xAg_{44-x}(SR)₃₀⁴⁻ is the most abundant Ag₄₄-based multianion species. Under these conditions, the relative trianion intensity is less than 5%. We therefore regard the relative intensity of Au_xAg_{44-x}(SR)₃₀⁴⁻ intermediates as a representative of the progression of the exchange reaction.

A three-dimensional “heat-map” plot of *m/z* versus reaction time showing the relative intensities of the Ag₄₄(SR)₃₀⁴⁻ starting clusters as well as the intermediate alloy cluster products is shown in Figure 1 (deconvoluted mass peaks are

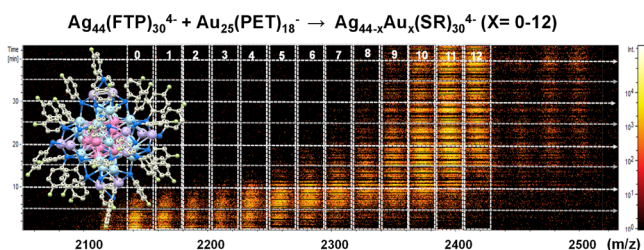


Figure 1. Time-dependent overview mass spectra of *intercluster* reaction showing slow formation of Au₁₂Ag₃₂(SR)₃₀⁴⁻ over 40 min reaction time for 5:1 Ag₄₄/Au₂₅ molar ratio (5 μM:1 μM); note the logarithmic intensity scale. Corresponding higher-resolution mass spectra are shown in Figure S1. The DFT-optimized structure of Ag₄₄(FTP)₃₀⁴⁻ is shown in the inset. See Figure 4 for structural details. Colors: Ag on the staple: light purple, Ag in shell: light cyan, Ag in the core: light pink, S: blue, C: light gray, and F: light green. Numbers 0, 1, 2...12 in the figure refer to the number of exchanges (*x*) in the reaction mentioned on the top.

shown in Figure S3). It is clear from the heat map that the initial reaction proceeds primarily via formation and subsequent consumption of intermediates with stepwise

exchange of silver by gold atoms (together with some exchange of ligands—see below). After a reaction time of 40 min, the composition change is essentially completed with predominantly Au₁₂Ag₃₂(SR)₃₀⁴⁻ cluster ions being detected. We infer that this corresponds to an exchange equilibrium in solution. This is supported by (i) the observation of reverse exchange upon adding more Ag₄₄(SR)₃₀⁴⁻ starting clusters at later reaction times and (ii) previous mass spectrometric probes of the corresponding Au_{25-x}Ag_x(SR)₁₈⁻ side of the reaction.²⁴

Several measurement series at different starting concentration ratios were conducted, and the typical kinetic plots are shown in Figures S4 and S5. A full kinetic analysis will be reported elsewhere. Here, we only note that as in previous reports, we find a highly nonstatistical, Au_xAg_{44-x}(SR)₃₀⁴⁻ final product distribution. In particular, we find a 6-fold enrichment in average gold content relative to a binomial distribution weighted with the initial Ag/Au atomic concentration ratio. Furthermore, the mixed cluster mass distribution is much narrower than binomial and essentially cut off beyond 12 substituted Au atoms (Figure S6). The predominance of Au₁₂Ag₃₂(SR)₃₀⁴⁻ supports previous conclusions that this composition is an island of low relative free energy among Au_xAg_{44-x}(SR)₃₀⁴⁻ species accessed.

Among the initial Ag₄₄/Au₂₅ concentration ratios studied, ranging from 5:1 to 20:1, 5:1 resulted in maximum equilibrium conversion to Ag₃₂Au₁₂(SR)₃₀⁴⁻ and was therefore chosen for further study. After recording the reaction kinetics by measuring mass-resolved ion intensity versus time, detailed trapped ion mobility measurements (TIMS) were performed to observe corresponding structural changes. Interestingly, we found that the CCSs of specific Au_xAg_{44-x}(SR)₃₀⁴⁻ cluster ions, *x* = 1–12, changed measurably during the course of the reaction.

Figure 2 shows representative contour plots of Au_xAg_{44-x}(SR)₃₀⁴⁻ ion intensity as functions of composition (*x* = 0–12) and CCS—for eight different reaction time intervals, A–H. These are based on the extracted TIMS

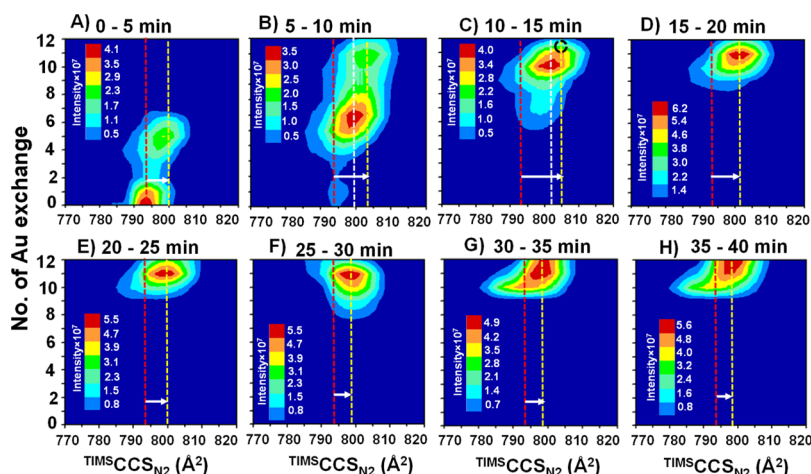


Figure 2. (A–H) Two-dimensional plots of time-dependent change in CCS during Au exchange into Ag₄₄(SR)₃₀⁴⁻ clusters to form Au_xAg_{44-x}(SR)₃₀⁴⁻, *x* = 1–12. Initially, the CCS of all intermediate *x* species increases till ca. 20 min of reaction time whereupon their CCS gradually shrinks as exchange equilibrium is approached (with a product distribution centered at *x* = 11 and 12). The red dashed line corresponds to the CCS (peak maximum in corresponding mobilogram) of unreacted Ag₄₄(SR)₃₀⁴⁻ (793 Å²). The yellow dashed lines correspond to the peak maximum CCS of the exchange product with the largest CCS in that time interval. The white dashed lines in (B,C) correspond to the peak maximum CCS of the most intense Au exchange product in the specified time interval. The position of the CCS peak maximum for 12 Au-exchanged product has been circled for clarity. Corresponding mobilograms (i.e., intensity vs CCS) are shown in Figure S7.

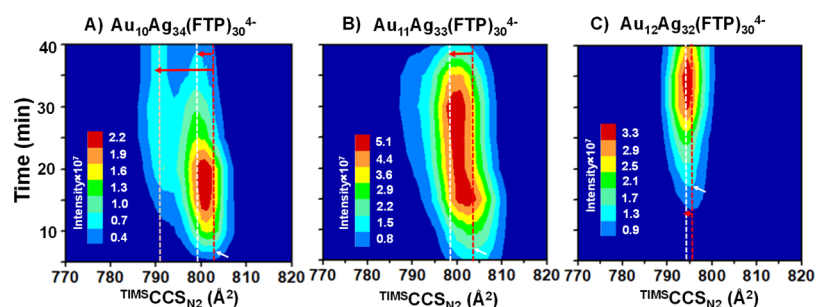


Figure 3. Time-dependent changes in the CCS of (A) $\text{Au}_{10}\text{Ag}_{34}(\text{FTP})_{30}^{4-}$, (B) $\text{Au}_{11}\text{Ag}_{33}(\text{FTP})_{30}^{4-}$, and (C) $\text{Au}_{12}\text{Ag}_{32}(\text{FTP})_{30}^{4-}$ are shown as contour plots. Each of the mobilograms was extracted for the corresponding mass range to include only contributions from 0 to 1 ligand-exchange products. The CCS values of $\text{Au}_{10}\text{Ag}_{34}(\text{FTP})_{30}^{4-}$ and $\text{Au}_{11}\text{Ag}_{33}(\text{FTP})_{30}^{4-}$ change significantly with time while the CCS of $\text{Au}_{12}\text{Ag}_{32}(\text{FTP})_{30}^{4-}$ remained almost constant. The red dashed lines correspond to the CCS of the respective products at the earliest reaction times at which they are detectable. The white/yellow dashed lines correspond to their final CCS. The initial CCS peak maximum of each species is indicated with a white arrow for clarity. Corresponding CCS vs normalized intensity plots are shown in Figure S11.

mobilograms (inverse mobility vs intensity plots) in N_2 collision gas (shown in Figure S7) obtained for each of the different $\text{Au}_x\text{Ag}_{44-x}(\text{SR})_{30}^{4-}$ masses, that is, for each discrete exchange product, at various reaction times following mixing of the silver and gold cluster reactants [under the same optimum solution reaction conditions as used for Figure 1 (5:1 $\text{Ag}_{44}/\text{Au}_{25}$ ratio)]. Corresponding instrumental details are described in a separate section below and further in the Supporting Information. Here, it is only important to realize that under our experimental conditions, we typically achieved ion mobility resolutions of 160 or better—with relative accuracies sufficient to distinguish $\text{TIMS CCS}_{\text{N}_2}$ differences of 0.2%.⁴⁷

Unreacted $\text{Ag}_{44}(\text{SR})_{30}^{4-}$ ions in gas phase have an experimental CCS of 793 \AA^2 . We assume that this corresponds to that of the most stable isomer/conformer under the given experimental conditions. It is unclear to what extent the isolated $\text{Ag}_{44}(\text{SR})_{30}^{4-}$ structure (determined by TIMS, some milliseconds after electrospraying) differs from that of the same species in solution. For simplicity, we shall assume that any such differences between solution and gas-phase structures are similar for all $\text{Au}_x\text{Ag}_{44-x}(\text{SR})_{30}^{4-}$, that is, changes in CCS reflect changes to the cluster structures during reaction in solution.

During the reaction, we first observe a sequential increase in CCS with increasing Au exchange. Specifically, we find that at reaction times of 10–15 min, the experimental CCS has increased from 793 \AA^2 for the $\text{Ag}_{44}(\text{SR})_{30}^{4-}$ reactant up to 805 \AA^2 for $\text{Au}_{10}\text{Ag}_{34}(\text{SR})_{30}^{4-}$ (~1.5% increase). Also, the corresponding mobilograms become significantly broader with increasing Au exchange compared to the unreacted $\text{Ag}_{44}(\text{SR})_{30}^{4-}$ (both effects can be seen more clearly in Figure S7, which plots ion intensity vs CCS for various reaction times and compositions). Interestingly, as the reaction proceeds further, we observe that the trend in CCS increases and the peak broadening reverses slightly (Figure 3). Specifically, the final CCS for $\text{Au}_{12}\text{Ag}_{32}(\text{SR})_{30}^{4-}$ was 799 \AA^2 . By contrast, the less abundant products with 9 and 10 Au exchanges retain a significantly broader mobilogram till the end of the reaction at 40 min.

There are two aspects which could lead to broadening of the mobilograms. First, $\text{Au}_{25}(\text{PET})_{18}^{-}$ clusters have a slightly larger ligand than $\text{Ag}_{44}(\text{FTP})_{30}^{4-}$. Hence, $\text{FTP} \rightarrow \text{PET}$ ligand exchange on the cluster surface²⁴ would be expected to increase the effective cross section of the ion by approximately 2 \AA^2 per ligand (Figure S8). Consequently, for a 12 \AA^2 increase, at least six ligand exchanges are necessary. To avoid

this issue, the mobilograms shown in Figures S9 and S10 which are used for the contour plots shown in Figures 2 and 3 were extracted from the lower mass flanks (left side) of the specific $\text{Au}_x\text{Ag}_{44-x}(\text{SR})_{30}^{4-}$ envelopes, that is, they correspond to 0–2 ligand exchanges (see Figure S7 in the Supporting Information for details). Therefore, the observed increase in CCS of up to 12 \AA^2 from $\text{Ag}_{44}(\text{SR})_{30}^{4-}$ to $\text{Au}_{10}\text{Ag}_{34}(\text{SR})_{30}^{4-}$ can not only be due to ligand exchange. As a corollary, this increase and the associated broadening of the respective mobilograms (see also Figures S7 and S8 in the Supporting Information) must reflect the structural change in order to accommodate the incoming Au and outgoing Ag. It seems likely that this would be associated with multiple isomeric forms having slightly different CCS simultaneously present during the reaction. As the Au/Ag exchange must start from the surface, the initial broadening is likely due to structural distortion of the staples. Over time, the Au atoms migrate from the “surface” and are collected in the core. Most likely as a result of this, the mobilograms of the 12 Au exchange product again becomes narrower and comparable with that of the unreacted $\text{Ag}_{44}(\text{FTP})_{30}^{4-}$ ion.

To obtain further information on the migration of Au atoms from the surface to the core and the associated (consecutive) structural reorganization, we analyzed the time-dependent CCS of the main products, $\text{Au}_x\text{Ag}_{44-x}(\text{SR})_{30}^{4-}$ ($x = 10$ –12) more carefully. The respective measurements are shown in Figure 3. Again, to avoid effects due to ligand exchange, mobilograms were extracted only over a mass range comprising at most one exchanged ligand. Upon its initial formation (at ca. 15 min), the CCS of $\text{Au}_{10}\text{Ag}_{34}(\text{SR})_{30}^{4-}$ was found to be 803 \AA^2 , shifting to lower values over time. After a reaction time of around 30 min, the peak maximum has decreased to 799 \AA^2 . Along with this shift in CCS of the main peak, another peak started to appear, which intensified over time. Its CCS value was found to be 791 \AA^2 , which is close to the CCS of the unreacted $\text{Ag}_{44}(\text{FTP})_{30}^{4-}$. This clearly shows the presence of two isomeric forms of $\text{Au}_{10}\text{Ag}_{34}(\text{SR})_{30}^{4-}$. The larger, less-compact one is likely distorted because of nonuniform Au exchange in different layers of the cluster (see later). Note that the differences in Au–Au/Au–S/Au–Ag bond lengths versus the corresponding Ag–Ag/and Ag values are quite small. Therefore, a compact, high-symmetry form of $\text{Au}_{10}\text{Ag}_{32}(\text{SR})_{30}^{4-}$ with all Au atoms in the core would be expected to have an overall CCS very similar to that of $\text{Ag}_{44}(\text{FTP})_{30}^{4-}$ (793 \AA^2). The slight decrease (2 \AA^2) in the

overall CCS for the more compact isomer could be due to different charge distributions among 10 Au and 2 Ag in the core. A similar trend was also observed for $\text{Au}_{11}\text{Ag}_{33}(\text{SR})_{30}^{4-}$, where after 15 min, the overall CCS and peak width decreased with further reaction time to yield a final CCS of 799 \AA^2 with a shoulder at 790 \AA^2 . Note that such shifts in CCS are also likely contributed to reorientation of the FTP ligands. Presumably, these rearrange slightly upon migration of Au from the surface to the core (the bond lengths and angles associated with Au–S vs Ag–S links are slightly different).

While $x = 10$ and 11 exchange products were formed almost immediately after mixing, $\text{Au}_{12}\text{Ag}_{32}(\text{SR})_{30}^{4-}$ began to be observed in significant amounts only after 20 min. Interestingly, this product does not show any significant change in its CCS [the final CCS was found to be 794 \AA^2 comparable to 793 \AA^2 for the parent $\text{Ag}_{44}(\text{FTP})_{30}^{4-}$]. Note that this observation is consistent with the time-dependent structural change of $x = 10$ and 11. After 20 min, the CCS of both the compact isomer of $\text{Au}_{10}\text{Ag}_{34}(\text{SR})_{30}^{4-}$ and the main part of $\text{Au}_{11}\text{Ag}_{33}(\text{SR})_{30}^{4-}$ was already comparable with their final CCS values. Hence, we infer that some clusters can already exchange and rearrange on this timescale to achieve a compact 12 gold atom core structure.

Next, we consider the molecular structure of $\text{Ag}_{44}(\text{FTP})_{30}$ in more detail. As already pointed out in the introduction, it comprises 12 Ag atoms in an inner hollow icosahedral core, which is surrounded by a shell of another 20 Ag atoms together forming a 32 (12@20) Ag atom core–shell entity. The remaining 12 Ag atoms are situated on the outer protecting staples as $6 \times \text{Ag}_2(\text{FTP})_5$ mounts.⁴⁸ In the simple Jellium model based on s -electron counting scheme initially proposed to explain local stability islands among bare alkali cluster sizes,^{3,4} which is also extensively used for monolayer-protected metal clusters, $\text{Ag}_{44}(\text{SR})_{30}^{4-}$ is a *closed electronic shell species* comprising $12 + 20 + 12 - 30 + 4 = 18$ s -electrons, that is, having the configuration $1S^2 + 1P^6 + 1D^{10}$ in the nomenclature of the spherical Jellium model. Our TIMS measurements suggest that the exchange of 12 Ag by 12 Au atoms starts at the surface and leads finally to a stable $\text{Au}_{12}\text{Ag}_{32}(\text{FTP})_{30}^{4-}$ isomer in which all 12 Au atoms reside in the hollow icosahedral core. To explore this further, we calculated three different isomers of $\text{Au}_{12}\text{Ag}_{32}(\text{FTP})_{30}^{4-}$ by DFT—using starting geometries based on the known crystal structure of $[\text{PPh}_4]_4\text{Ag}_{44}(\text{FTP})_{30}$. For the first isomer (I), all Au atoms were assumed to occupy the hollow icosahedral core. For the second isomer (S—“statistically” distributed), the 12 Au atoms were equally, but otherwise randomly, distributed throughout the three different regions of the metal cluster (in the core, in the middle shell, and among the outer staples—four atoms each). In the final isomer (M), all 12 Au atoms were positioned in the outer staples (mount position) (Figure 4).

Isomer I is the most stable one ($E = 0 \text{ eV}$) followed by isomer S ($E = 2.8 \text{ eV}$) and then isomer M ($E = 5.8 \text{ eV}$) as also predicted by previous DFT calculations and consistent with the crystal structure determination of $[\text{PPh}_4]_4[\text{Au}_{12}\text{Ag}_{32}(\text{FTP})_{30}]$.²⁸ Based on the DFT results, the CCS of each of these isomers in N_2 as well as that of the parent $\text{Ag}_{44}(\text{FTP})_{30}^{4-}$ were modeled by trajectory calculations using IMoS 1.09⁴⁴ with the default Lennard-Jones parameters and charges based on NBO analysis (see the Experimental Section and ref 39). For $\text{Ag}_{44}(\text{FTP})_{30}^{4-}$, CCS_{NBO} was found to be 902.5 \AA^2 , while for the I-, M-, S-isomers of $\text{Au}_{12}\text{Ag}_{32}(\text{FTP})_{30}^{4-}$, the calculated CCS values were 901.3 , 911.0 , and 908.7 \AA^2 ,

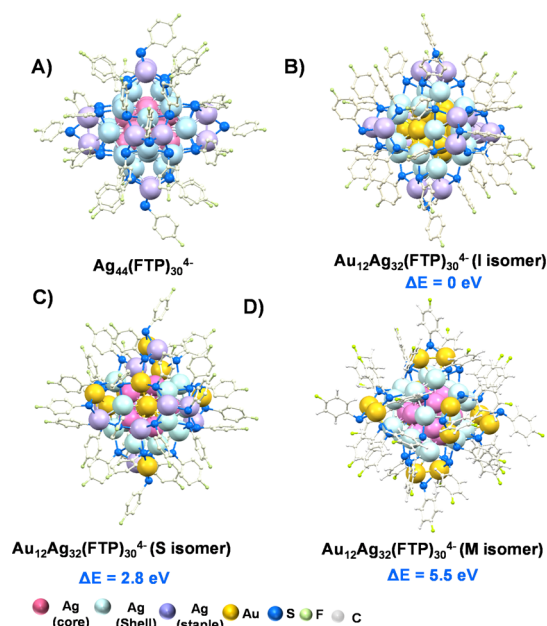


Figure 4. DFT-optimized structures of $\text{Ag}_{44}(\text{FTP})_{30}^{4-}$ and three different isomers of $\text{Au}_{12}\text{Ag}_{32}(\text{SR})_{30}^{4-}$ (relative energies in red). In all cases, 12 metal atoms are in the six staples (each terminated by five ligands), 20 metal atoms form a shell underneath within which 12 metal atoms reside in a hollow icosahedral core. Isomer I: all 12 Au atoms in the hollow inner icosahedron. Isomer S: four Au atoms statistically distributed in each of the three cluster layers. Isomer M: all 12 Au atoms in the staples.

respectively. The calculated CCS_{NBO} of $\text{Ag}_{44}(\text{FTP})_{30}^{4-}$ is 14% larger than the experimental value $^{\text{TIMS}}\text{CCS}_{\text{N}_2}$ (902.5 \AA^2 vs 793 \AA^2), which is a significantly larger difference than one might expect. The calculated CCS for highly charged species depends crucially on the partial charge distribution within the ion. The NBO analysis places quite high partial charges on each atom (up to 0.6, see the Supporting Information). Therefore, the calculation was repeated with two different charge distributions: first, the Mulliken population analysis was used which predicted even higher partial charges (up to 1.5). This resulted in CCS_{Mul} values of 905.9 \AA^2 for $\text{Ag}_{44}(\text{FTP})_{30}^{4-}$ and 905.9 , 920.5 , and 914.7 \AA^2 for the I-, M-, and S-isomers of $\text{Au}_{12}\text{Ag}_{32}(\text{FTP})_{30}^{4-}$, respectively, that is, between 0.4 and 1.0% larger than the NBO-based CCS_{NBO} . Second, the 4-fold negative charge was put into the (hollow) center of the cluster, leaving the individual atoms uncharged. Under this extreme assumption, $\text{CCS}_{\text{center}}$ was found to be 860.5 for $\text{Ag}_{44}(\text{FTP})_{30}^{4-}$ and 858.6 , 875.5 , and 867.1 \AA^2 for the I-, M-, and S-isomers of $\text{Au}_{12}\text{Ag}_{32}(\text{FTP})_{30}^{4-}$, that is, roughly 8% above the experimental values. In other words, these calculations show that the charge distribution has a large effect on the calculated CCS and that $\text{CCS}_{\text{center}}$ fits better than NBO or Mulliken. However, the CCS difference between experiment and calculation remains rather large, independent of the charge placement algorithm. This is possibly a reflection of other systematic errors in the TM calculations (e.g., because of default parameterized metal atoms). To take this into account, an empirical scaling factor (0.879) was used to calibrate the calculated CCS_{NBO} of 902.5 \AA^2 against the experimental $^{\text{TIMS}}\text{CCS}_{\text{N}_2}$ 793 \AA^2 value. Using the same scaling factor for the three isomers of $\text{Au}_{12}\text{Ag}_{32}(\text{FTP})_{30}^{4-}$, $^{\text{corr}}\text{CCS}_{\text{NBO}}$ was found to be 793.1 , 800.8 , and 798.7 \AA^2 for isomers I, M, and S, respectively.

Table 1. Comparison of Experimental ${}^{\text{TIMS}}\text{CCS}_{\text{N}_2}$ Values with CCS Trajectory Calculations Based on DFT-Optimized Structures as Shown in Figure 4^a

ions	experimental CCS (\AA^2)	calculated CCS_{NBO} (\AA^2)	calculated $\text{CCS}_{\text{center}}$ (\AA^2)	calculated ${}^{\text{corr}}\text{CCS}_{\text{NBO}}$ (\AA^2)	calculated ${}^{\text{corr}}\text{CCS}_{\text{center}}$ (\AA^2)
$\text{Ag}_{44}(\text{FTP})_{30}^{4-}$	793	902.5	860.5	793.3	793.4
$\text{Au}_{12}\text{Ag}_{32}(\text{FTP})_{30}^{4-}$ (I) (0 eV)	794	901.3	858.6	793.1	791.6
$\text{Au}_{12}\text{Ag}_{32}(\text{FTP})_{30}^{4-}$ (S) (2.8 eV)		911.0	875.5	800.8	807.2
$\text{Au}_{12}\text{Ag}_{32}(\text{FTP})_{30}^{4-}$ (M) (5.5 eV)		908.7	867.1	798.7	799.5

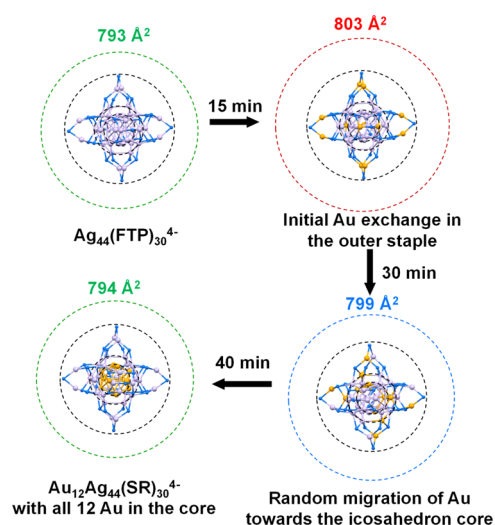
^aThe trajectory calculations using IMoS 1.09 were performed with two different assumptions concerning (excess) charge localization, CCS_{NBO} , and $\text{CCS}_{\text{center}}$; see main text for details. ${}^{\text{corr}}\text{CCS}$ values were scaled against the experimental value for $\text{Ag}_{44}(\text{FTP})_{30}^{4-}$. Using exact hard spheres scattering method which completely neglects charges, similar CCS values as with the TM (with the charge localized in the center) were obtained.

Apparently, the lowest energy isomer I fits best to the experimental ${}^{\text{TIMS}}\text{CCS}_{\text{N}_2}$ value of 794 \AA^2 . Scaling the CCS calculated with the central charge ($\text{CCS}_{\text{center}}$) in an analogous fashion by 0.922 (to match the experimental ${}^{\text{TIMS}}\text{CCS}_{\text{N}_2}$ of $\text{Ag}_{44}(\text{FTP})_{30}^{4-}$) results in ${}^{\text{corr}}\text{CCS}_{\text{center}}$ values of 791.6, 807.2, and 799.5 \AA^2 (I, M, and S)—again isomer I fits the best. Therefore, the isomer assignment is rather robust with respect to the method used. The results are summarized in Table 1.

The DFT + IMoS-based modeling of the CCS measurements therefore supports our inference that the approximately 1% increase in the CCS observed for $\text{Au}_x\text{Ag}_{44-x}(\text{SR})_{30}^{4-}$ ($x = 10, 11$) at a reaction time of 10 min—relative to the CCS of the parent cluster—reflects the initial Au/Ag exchange on the staples. This CCS increase is similar to the 1.2% larger CCS of the M isomer of $\text{Au}_{12}\text{Ag}_{32}(\text{SR})_{30}^{4-}$ versus $\text{Au}_{44}(\text{SR})_{30}^{4-}$. Similarly, the significant CCS decrease subsequently observed in particular for $x = 10$ and 11 can be related to the S isomer of $\text{Au}_{12}\text{Ag}_{32}(\text{SR})_{30}^{4-}$. This is 0.7% larger than the parent $\text{Ag}_{44}(\text{FTP})_{30}^{4-}$. Note that S isomer is considered as a model for an intermediate rather than the actual one. Once the reaction reaches equilibrium and the 12 Au atom exchange product dominates in intensity, the CCS of $\text{Au}_{12}\text{Ag}_{32}(\text{SR})_{30}^{4-}$ was found to be 794 \AA^2 , which is almost identical to that of the parent $\text{Ag}_{44}(\text{FTP})_{30}^{4-}$ and is in good agreement with isomer I. Consequently, we experimentally resolve the migration of Au atoms from the staples to the cluster core (see Scheme 1)—a process which can apparently occur on a ca. 10 min timescale in room-temperature solutions.

To obtain further insight into Au atom migration, CID measurements were performed for each of the Au exchange products, $\text{Au}_x\text{Ag}_{44-x}(\text{SR})_{30}^{4-}$ ($x = 0-12$), with varying collision energy. Solution concentrations, concentration ratios, and reaction times differed slightly from those used for timsTOF so as to obtain optimal signal intensities. Typically, $x = 1-5$ exchange products were probed by CID after relatively short reaction times to obtain sufficient signals and for $x = 6-12$ after longer reaction times allowing for structural equilibration. All the CID experiments were performed on the Waters' SYNAPT G2S platform in slightly higher than regular trap gas flow (5 mL/min instead of regular 2 mL/min) to access a larger lab frame collision energy range.⁴⁹ To analyze the data, the laboratory collision energy settings were converted to center-of-mass energy (assuming a single ion/Ar collision) and the energy values corresponding to 50% survival yield were then determined ($=E_{\text{com}(50)}$). The corresponding numbers are shown in Figures S12–S15. Note that in the absence of calibration measurements with structurally related thermometer ions,⁵⁰ the collision energy settings and thus the resulting $E_{\text{com}(50)}$ values are only relative

Scheme 1. Schematic of Au Atom Migration from the Outer Staple to the Inner core^a



^aLigands are not shown for clarity (apart from the S atoms). The ligand layer is represented by the outermost dashed circle to signify the range of the ligand shell whose diameter increases in the order green \rightarrow blue \rightarrow red during Au exchange and subsequent migration. Colors: Ag: purple, Au: orange, and S: blue.

numbers, that is, for comparison between different $x = 0-12$. They are not absolute dissociation energy determinations. With this caveat in mind, the $E_{\text{com}(50)}$ values of 0.225 and 0.286 eV for $\text{Ag}_{44}(\text{FTP})_{30}^{4-}$ and $\text{Au}_{12}\text{Ag}_{32}(\text{SR})_{30}^{4-}$, respectively, confirm the lower relative stability of the parent $\text{Ag}_{44}(\text{FTP})_{30}^{4-}$. The corresponding $E_{\text{com}(50)}$ determination for $\text{Au}_{12}\text{Ag}_{32}(\text{SR})_{30}^{4-}$ is shown in Figure S12B. A plot of $E_{\text{com}(50)}$ values versus $x = 0-12$ is shown in Figure S12C. Although there is no clear monotonic dependence on x (within the noise of the measurements), $E_{\text{com}(50)}$ values are systematically >0.225 eV, that is, Au exchange always leads to stabilization relative to $\text{Ag}_{44}(\text{FTP})_{30}^{4-}$.

For $\text{Ag}_{44}(\text{FTP})_{30}^{4-}$, the main fragmentation pathway involves $\text{Ag}(\text{FTP})_2^-$ (m/z 362) loss (see Figure S12A). In all Au exchange products, an additional fragment peak appears at m/z 451, which can be assigned to the corresponding $\text{Au}(\text{FTP})_2^-$ loss channel. In Figure S12D, we have plotted the normalized intensity of the m/z 451 fragment signal (at a constant laboratory collision energy setting of 6 V) against $x = 0-12$. It is evident that for higher x , the $\text{Au}(\text{FTP})_2^-$ fragment intensity increases. This is surprising at first glance: if all Au atoms occupy the I position (i.e., located in the central icosahedron) and only the “staples” at the clusters surface are

involved in fragmentation, one would expect to see just $\text{Ag}(\text{FTP})_2^-$ loss. Clearly, some Au atoms must be transported back to the staples after collisional energization. Our experimental time window during which subsequent fragmentation can be detected is likely on the order of 100 μs . Consequently, we infer that at the vibrational temperatures generated upon collisions with Ar, the cluster forms a nanoalloy in which the heavier Au atoms can diffuse from the core to the cluster surface (staple) on the measurement timescale. In future work, it will be interesting to more quantitatively compare such observations to analogous in situ transmission electron microscopy studies of T-dependent redistribution upon alloying core–shell silver–gold nanoparticles.⁵¹

4. CONCLUSIONS

In summary, we have used time-dependent TIMS to probe the intercluster reactions between $\text{Ag}_{44}(\text{FTP})_{30}^{4-}$ and $\text{Au}_{25}(\text{PET})_{18}^-$ in room-temperature solutions. As silver and gold atoms are very similar in size, there is very little scope to understand the structural changes in such cluster systems arising from Ag/Au exchange. Nevertheless, we show here for the first time that the high resolution and relative accuracy of TIMS is sufficient to observe systematic, time-dependent changes in the CCSs of $\text{Au}_x\text{Ag}_{44-x}(\text{SR})_{30}^{4-}$ species. These can be assigned to migration of exchanging Au atoms from the cluster surface (staples/mount position) via the shell to the core on the 0–40 min timescale in the room-temperature solution mixture. Note that we have presented the simplest explanation which is still consistent with the experimental data. For this, the following set of assumptions has been made: (i) the electrosprayable $\text{Au}_x\text{Ag}_{44-x}(\text{SR})_{30}^{4-}$ tetra-anions probed (without fragmentation) are assumed to be representative intermediates in a complicated kinetic scheme; (ii) in particular, intermediates with only 0–1 ligand exchange have been considered for interpretation of experimental CCS changes while more ligand exchange is usual; and (iii) the reaction proceeds via single Ag/Au exchange at a time (no strong “even/odd” effect was found in the time-dependent mass spectra). In future work on this system, it will be interesting to look more closely at early stage exchange events by comparing the present results with analogous measurements on clusters carrying the same SR ligands.

Apparently, about two or more Au exchanges in the staples lead to a measurable increase in the CCS mainly because of the differences in Ag–S–ligand and Au–S–ligand arrangement. This effect reverts when Au atoms “submerge” into the intermediate shell/icosahedral core whereupon the Ag–S–ligand reassumes its original arrangement on the surface. The interdiffusion of Au/Ag in the shell \rightarrow core is observed at the resolution limit of TIMS. We do however see two isomers for $\text{Au}_{10}\text{Ag}_{34}(\text{SR})_{30}^{4-}$ and a low cross-sectional shoulder on $\text{Au}_{11}\text{Ag}_{33}(\text{SR})_{30}^{4-}$. By contrast, the CCS of $\text{Au}_{12}\text{Ag}_{32}(\text{SR})_{30}^{4-}$ does not change significantly over the reaction time of 20–40 min, and hence, here diffusion of Au from the shell to the core is not clearly visible (or perhaps for the $x = 12$ free energy minimum, it is just too fast to be observed by timsTOF). Upon collisional heating during tandem mass spectrometry, we observed predominantly $\text{Au}(\text{FTP})_2^-$ fragment which might imply analogous back-migration of the heavier Au atoms from the core to the staples. Our experimental observations are supported by DFT calculations of different isomeric structures. By determining the corresponding CCS values and comparing

them to experiment, we have been able to draw some first inferences concerning the migration mechanism. Thus, this study establishes high-resolution TIMS as a very useful method to study heteroatom doping of monolayer-protected atomically precise metal clusters in condensed phase.

■ ASSOCIATED CONTENT

Supporting Information

The Supporting Information is available free of charge on the ACS Publications website at DOI: 10.1021/acs.jpcc.9b08686.

Synthesis of $[\text{TOA}][\text{Au}_{25}(\text{PET})_{18}]$ and $[\text{PPh}_4]_4[\text{Ag}_{44}(\text{FTP})_{30}]$, instrumental parameters, concentration-dependent kinetics, plots of 50% survival yields of different Au-exchanged products, coordinates of DFT-optimized structures of $\text{Ag}_{44}(\text{FTP})_{30}^{4-}$, and different isomers of $\text{Au}_{12}\text{Ag}_{32}(\text{FTP})_{30}^{4-}$ with corresponding partial charges (PDF)

■ AUTHOR INFORMATION

Corresponding Authors

*E-mail: horst.hahn@kit.edu (H.H.).

*E-mail: pradeep@iitm.ac.in (T.P.).

*E-mail: manfred.kappes@kit.edu (M.M.K.).

ORCID

Ananya Baksi: 0000-0003-3328-4399

Patrick Weis: 0000-0001-7006-6759

Horst Hahn: 0000-0001-9901-3861

Thalappil Pradeep: 0000-0003-3174-534X

Manfred M. Kappes: 0000-0002-1199-1730

Author Contributions

A.B. and E.K.S. have performed the experiments and analyzed the data. DFT optimization and calculation of CCS were performed by P.W., A.B., and E.K.S. M.M.K. and A.B. have written the manuscript, which was refined by other authors. D.G. and K.R.K. have synthesized the clusters and helped in initial characterization of the clusters. The work was done in collaboration with T.P. and his group. All authors participated in the discussion and interpretation of the data. The whole project was supervised by M.M.K.

Notes

The authors declare no competing financial interest.

■ ACKNOWLEDGMENTS

M.M.K. and H.H. acknowledge the research support from the Helmholtz Association of German Research Centers through Program STN (Science and Technology of Nanosystems). Additionally, P.W. and M.M.K. thank KIT as well as the DFG-funded collaborative research center “3MET” (Project C6) for supporting the timsTOF implementation. T.P. thanks the Department of Science and Technology, India, for funding. H.H. acknowledges the financial support from German Academic Exchange Service (DAAD).

■ REFERENCES

- (1) Foster, P. J.; Leckenby, R. E.; Robbins, E. J. Ionization potentials of clustered alkali metal atoms. *Proc. Phys. Soc., London, At. Mol. Phys.* **1969**, *2*, 478–483.
- (2) Dietz, T. G.; Duncan, M. A.; Powers, D. E.; Smalley, R. E. Laser production of supersonic metal cluster beams. *J. Chem. Phys.* **1981**, *74*, 6511–6512.

- (3) Kappes, M. M.; Kunz, R. W.; Schumacher, E. Production of large sodium clusters (N_{ax} , $x \leq 65$) by seeded beam expansions. *Chem. Phys. Lett.* **1982**, *91*, 413–418.
- (4) Knight, W. D.; Clemenger, K.; De Heer, W. A.; Saunders, W. A.; Chou, M. Y.; Cohen, M. L. Electronic shell structure and abundances of sodium clusters. *Phys. Rev. Lett.* **1984**, *52*, 2141–2143.
- (5) Heaven, M. W.; Dass, A.; White, P. S.; Holt, K. M.; Murray, R. W. Crystal Structure of the Gold Nanoparticle $[N(C_8H_{17})_4][Au_{25}(SCH_2CH_2Ph)_{18}]$. *J. Am. Chem. Soc.* **2008**, *130*, 3754–3755.
- (6) Zhu, M.; Aikens, C. M.; Hollander, F. J.; Schatz, G. C.; Jin, R. Correlating the Crystal Structure of A Thiol-Protected Au₂₅ Cluster and Optical Properties. *J. Am. Chem. Soc.* **2008**, *130*, 5883–5885.
- (7) Negishi, Y.; Chaki, N. K.; Shichibu, Y.; Whetten, R. L.; Tsukuda, T. Origin of Magic Stability of Thiolated Gold Clusters: A Case Study on Au₂₅(SC₆H₁₃)₁₈. *J. Am. Chem. Soc.* **2007**, *129*, 11322–11323.
- (8) Brust, M.; Walker, M.; Bethell, D.; Schiffrin, D. J.; Whyman, R. Synthesis of thiol-derivatized gold nanoparticles in a two-phase liquid-liquid system. *J. Chem. Soc., Chem. Commun.* **1994**, 801–802.
- (9) Gilroy, K. D.; Ruditskiy, A.; Peng, H.-C.; Qin, D.; Xia, Y. Bimetallic Nanocrystals: Syntheses, Properties, and Applications. *Chem. Rev.* **2016**, *116*, 10414–10472.
- (10) Jin, R.; Zeng, C.; Zhou, M.; Chen, Y. Atomically Precise Colloidal Metal Nanoclusters and Nanoparticles: Fundamentals and Opportunities. *Chem. Rev.* **2016**, *116*, 10346–10413.
- (11) Yan, J.; Teo, B. K.; Zheng, N. Surface Chemistry of Atomically Precise Coinage-Metal Nanoclusters: From Structural Control to Surface Reactivity and Catalysis. *Acc. Chem. Res.* **2018**, *51*, 3084–3093.
- (12) Krishnadas, K. R.; Natarajan, G.; Bakshi, A.; Ghosh, A.; Khatun, E.; Pradeep, T. Metal-Ligand Interface in the Chemical Reactions of Ligand-Protected Noble Metal Clusters. *Langmuir* **2019**, *35*, 11243.
- (13) Krishnadas, K. R.; Bakshi, A.; Ghosh, A.; Natarajan, G.; Som, A.; Pradeep, T. Interparticle Reactions: An Emerging Direction in Nanomaterials Chemistry. *Acc. Chem. Res.* **2017**, *50*, 1988–1996.
- (14) Chakraborty, I.; Pradeep, T. Atomically Precise Clusters of Noble Metals: Emerging Link between Atoms and Nanoparticles. *Chem. Rev.* **2017**, *117*, 8208–8271.
- (15) Wang, S.; Li, Q.; Kang, X.; Zhu, M. Customizing the Structure, Composition, and Properties of Alloy Nanoclusters by Metal Exchange. *Acc. Chem. Res.* **2018**, *51*, 2784–2792.
- (16) Hossain, S.; Ono, T.; Yoshioka, M.; Hu, G.; Hosoi, M.; Chen, Z.; Nair, L. V.; Niihori, Y.; Kurashige, W.; Jiang, D.-e.; Negishi, Y. Thiolate-protected trimetallic Au₂₀Ag₄Pd and Au²⁰Ag₄Pt alloy clusters with controlled chemical composition and metal positions. *J. Phys. Chem. Lett.* **2018**, *9*, 2590–2594.
- (17) Wang, S.; Song, Y.; Jin, S.; Liu, X.; Zhang, J.; Pei, Y.; Meng, X.; Chen, M.; Li, P.; Zhu, M. Metal Exchange Method Using Au₂₅ Nanoclusters as Templates for Alloy Nanoclusters with Atomic Precision. *J. Am. Chem. Soc.* **2015**, *137*, 4018–4021.
- (18) Yang, S.; Wang, S.; Jin, S.; Chen, S.; Sheng, H.; Zhu, M. A metal exchange method for thiolate-protected tri-metal M₁Ag_xAu_{24-x}(SR)₁₈ (M = Cd/Hg) nanoclusters. *Nanoscale* **2015**, *7*, 10005–10007.
- (19) Li, Q.; Luo, T.-Y.; Taylor, M. G.; Wang, S.; Zhu, X.; Song, Y.; Mpourmpakis, G.; Rosi, N. L.; Jin, R. Molecular “surgery” on a 23-gold-atom nanoparticle. *Sci. Adv.* **2017**, *3*, No. e1603193.
- (20) Alkan, F.; Pandeya, P.; Aikens, C. M. Understanding the Effect of Doping on Energetics and Electronic Structure for Au₂₅, Ag₂₅, and Au₃₈ Clusters. *J. Phys. Chem. C* **2019**, *123*, 9516–9527.
- (21) Li, Y.; Luo, T.-Y.; Zhou, M.; Song, Y.; Rosi, N. L.; Jin, R. A Correlated Series of Au/Ag Nanoclusters Revealing the Evolutionary Patterns of Asymmetric Ag Doping. *J. Am. Chem. Soc.* **2018**, *140*, 14235–14243.
- (22) Krishnadas, K. R.; Bakshi, A.; Ghosh, A.; Natarajan, G.; Pradeep, T. Structure-conserving spontaneous transformations between nanoparticles. *Nat. Commun.* **2016**, *7*, 13447.
- (23) Krishnadas, K. R.; Bakshi, A.; Ghosh, A.; Natarajan, G.; Pradeep, T. Manifestation of Geometric and Electronic Shell Structures of Metal Clusters in Intercluster Reactions. *ACS Nano* **2017**, *11*, 6015–6023.
- (24) Krishnadas, K. R.; Ghosh, A.; Bakshi, A.; Chakraborty, I.; Natarajan, G.; Pradeep, T. Intercluster Reactions between Au₂₅(SR)₁₈ and Ag₄₄(SR)₃₀. *J. Am. Chem. Soc.* **2016**, *138*, 140–148.
- (25) Krishnadas, K. R.; Ghosh, D.; Ghosh, A.; Natarajan, G.; Pradeep, T. Structure-Reactivity Correlations in Metal Atom Substitutions of Monolayer-Protected Noble Metal Alloy Clusters. *J. Phys. Chem. C* **2017**, *121*, 23224–23232.
- (26) Bakshi, A.; Chakraborty, P.; Bhat, S.; Natarajan, G.; Pradeep, T. [Au₂₅(SR)₁₈]₂₂: a noble metal cluster dimer in the gas phase. *Chem. Commun.* **2016**, *52*, 8397–8400.
- (27) Chakraborty, P.; Bakshi, A.; Mudedla, S. K.; Nag, A.; Paramasivam, G.; Subramanian, V.; Pradeep, T. Understanding proton capture and cation-induced dimerization of [Ag₂₉(BDT)₁₂]₃-clusters by ion mobility mass spectrometry. *Phys. Chem. Chem. Phys.* **2018**, *20*, 7593–7603.
- (28) Yang, H.; Wang, Y.; Huang, H.; Gell, L.; Lehtovaara, L.; Malola, S.; Hakkinen, H.; Zheng, N. All-thiol-stabilized Ag₄₄ and Au₁₂Ag₃₂ nanoparticles with single-crystal structures. *Nat. Commun.* **2013**, *4*, 2422.
- (29) Su, H.; Wang, Y.; Ren, L.; Yuan, P.; Teo, B. K.; Lin, S.; Zheng, L.; Zheng, N. Fractal Patterns in Nucleation and Growth of Icosahedral Core of [Au_nAg_{44-n}(SC₆H₅F₂)₃₀]₄ (n = 0–12) via ab Initio Synthesis: Continuously Tunable Composition Control. *Inorg. Chem.* **2019**, *58*, 259–264.
- (30) Yao, Q.; Feng, Y.; Fung, V.; Yu, Y.; Jiang, D.-e.; Yang, J.; Xie, J. Precise control of alloying sites of bimetallic nanoclusters via surface motif exchange reaction. *Nat. Commun.* **2017**, *8*, 1555.
- (31) Zhang, B.; Salassa, G.; Bürgi, T. Silver migration between Au₃₈(SC₂H₄Ph)₂₄ and doped Ag_xAu_{38-x}(SC₂H₄Ph)₂₄ nanoclusters. *Chem. Commun.* **2016**, *52*, 9205–9207.
- (32) Chakraborty, P.; Nag, A.; Natarajan, G.; Bandyopadhyay, N.; Paramasivam, G.; Panwar, M. K.; Chakrabarti, J.; Pradeep, T. Rapid isotopic exchange in nanoparticles. *Sci. Adv.* **2019**, *5*, No. eaau7555.
- (33) Bertorelle, F.; Russier-Antoine, I.; Comby-Zerbino, C.; Chirot, F.; Dugourd, P.; Brevet, P.-F.; Antoine, R. Isomeric Effect of Mercaptobenzoic Acids on the Synthesis, Stability, and Optical Properties of Au₂₅(MBA)₁₈ Nanoclusters. *ACS Omega* **2018**, *3*, 15635–15642.
- (34) Comby-Zerbino, C.; Bertorelle, F.; Chirot, F.; Dugourd, P.; Antoine, R. Structural insights into glutathione-protected gold Au₁₀₋₁₂(SG)₁₀₋₁₂ nanoclusters revealed by ion mobility mass spectrometry. *Eur. Phys. J. D* **2018**, *72*, 144.
- (35) Daly, S.; Choi, C. M.; Zavras, A.; Krstić, M.; Chirot, F.; Connell, T. U.; Williams, S. J.; Donnelly, P. S.; Antoine, R.; Giuliani, A.; Bonačić-Koutecký, V.; Dugourd, P.; O’Hair, R. A. J. Gas-Phase Structural and Optical Properties of Homo- and Heterobimetallic Rhombic Dodecahedral Nanoclusters [Ag_{14-n}Cu_n(C≡CtBu)₁₂X]⁺ (X = Cl and Br): Ion Mobility, VUV and UV Spectroscopy, and DFT Calculations. *J. Phys. Chem. C* **2017**, *121*, 10719–10727.
- (36) Bakshi, A.; Harvey, S. R.; Natarajan, G.; Wysocki, V. H.; Pradeep, T. Possible isomers in ligand protected Ag₁₁ cluster ions identified by ion mobility mass spectrometry and fragmented by surface induced dissociation. *Chem. Commun.* **2016**, *52*, 3805–3808.
- (37) Bakshi, A.; Ghosh, A.; Mudedla, S. K.; Chakraborty, P.; Bhat, S.; Mondal, B.; Krishnadas, K. R.; Subramanian, V.; Pradeep, T. Isomerism in Monolayer Protected Silver Cluster Ions: An Ion Mobility-Mass Spectrometry Approach. *J. Phys. Chem. C* **2017**, *121*, 13421–13427.
- (38) Bhat, S.; Bakshi, A.; Mudedla, S. K.; Natarajan, G.; Subramanian, V.; Pradeep, T. Au₂₂Ir₃(PET)₁₈: An Unusual Alloy Cluster through Intercluster Reaction. *J. Phys. Chem. Lett.* **2017**, *8*, 2787–2793.
- (39) Becke, A. D. Density-functional exchange-energy approximation with correct asymptotic behavior. *Phys. Rev. A: At., Mol., Opt. Phys.* **1988**, *38*, 3098–3100.
- (40) Perdew, J. P. Density-functional approximation for the correlation energy of the inhomogeneous electron gas. *Phys. Rev. B: Condens. Matter Mater. Phys.* **1986**, *33*, 8822–8824.

- (41) Weigend, F.; Ahlrichs, R. Balanced basis sets of split valence, triple zeta valence and quadruple zeta valence quality for H to Rn: Design and assessment of accuracy. *Phys. Chem. Chem. Phys.* **2005**, *7*, 3297–3305.
- (42) Furche, F.; Ahlrichs, R.; Hättig, C.; Klopper, W.; Sierka, M.; Weigend, F. Turbomole. *Wiley Interdiscip. Rev.: Comput. Mol. Sci.* **2014**, *4*, 91–100.
- (43) Reed, A. E.; Weinstock, R. B.; Weinhold, F. Natural population analysis. *J. Chem. Phys.* **1985**, *83*, 735–746.
- (44) Larriba, C.; Hogan, C. J. Ion Mobilities in Diatomic Gases: Measurement versus Prediction with Non-Specular Scattering Models. *J. Phys. Chem. A* **2013**, *117*, 3887–3901.
- (45) Larriba, C.; Hogan, C. J. Free molecular collision cross section calculation methods for nanoparticles and complex ions with energy accommodation. *J. Comput. Phys.* **2013**, *251*, 344–363.
- (46) Wu, T.; Derrick, J.; Nahin, M.; Chen, X.; Larriba-Andaluz, C. Optimization of long range potential interaction parameters in ion mobility spectrometry. *J. Chem. Phys.* **2018**, *148*, 074102.
- (47) Hennrich, F.; Schneider, E.; Weis, P.; Kappes, M. M. Comparing Empty and Filled Fullerene Cages with High-Resolution Trapped Ion Mobility Spectrometry. *J. Am. Soc. Mass Spectrom.* **2019**, *30*, 1973.
- (48) Desireddy, A.; Conn, B. E.; Guo, J.; Yoon, B.; Barnett, R. N.; Monahan, B. M.; Kirschbaum, K.; Griffith, W. P.; Whetten, R. L.; Landman, U.; Bigioni, T. P. Ultrastable silver nanoparticles. *Nature* **2013**, *501*, 399–402.
- (49) Chakraborty, P.; Baksi, A.; Khatun, E.; Nag, A.; Ghosh, A.; Pradeep, T. Dissociation of Gas Phase Ions of Atomically Precise Silver Clusters Reflects Their Solution Phase Stability. *J. Phys. Chem. C* **2017**, *121*, 10971–10981.
- (50) Brendle, K.; Kordel, M.; Schneider, E.; Wagner, D.; Bräse, S.; Weis, P.; Kappes, M. M. Collision Induced Dissociation of Benzylpyridinium-Substituted Porphyrins: Towards a Thermometer Scale for Multiply Charged Ions? *J. Am. Soc. Mass Spectrom.* **2018**, *29*, 382–392.
- (51) van der Hoeven, J. E. S.; Welling, T. A. J.; Silva, T. A. G.; van den Reijen, J. E.; La Fontaine, C.; Carrier, X.; Louis, C.; van Blaaderen, A.; de Jongh, P. E. In Situ Observation of Atomic Redistribution in Alloying Gold-Silver Nanorods. *ACS Nano* **2018**, *12*, 8467–8476.